

INVITED TOPICAL REVIEW

MODELING OF SUPERCRITICAL VAPORIZATION, MIXING, AND COMBUSTION PROCESSES IN LIQUID-FUELED PROPULSION SYSTEMS

VIGOR YANG

*The Pennsylvania State University
104 Research Building East
University Park, PA 16802 USA*

This paper addresses the physiochemical mechanisms involved in transcritical and supercritical vaporization, mixing, and combustion processes in contemporary liquid-fueled propulsion and power-generation systems. Fundamental investigation into these phenomena poses an array of challenges due to the obstacles in conducting experimental measurements and numerical simulations at scales sufficient to resolve the underlying processes. In addition to all of the classical problems for multiphase chemically reacting flows, a unique set of problems arises from the introduction of thermodynamic nonidealities and transport anomalies. The situation becomes even more complex with increasing pressure because of an inherent increase in the flow Reynolds number and difficulties that arise when fluid states approach the critical mixing condition. The paper attempts to provide an overview of recent advances in theoretical modeling and numerical simulation of this subject. A variety of liquid propellants, including hydrocarbon and cryogenic fluids, under both steady and oscillatory conditions, are treated systematically. Emphasis is placed on the development of a hierarchical approach and its associated difficulties. Results from representative studies are presented to lend insight into the intricate nature of the problem.

Introduction

Liquid droplet vaporization and spray combustion in supercritical environments have long been matters of serious practical concern in combustion science and technology, mainly due to the necessity of developing high-pressure combustion devices such as liquid-propellant rocket, gas-turbine, diesel, and pulse-detonation engines. Liquid fuels and/or oxidizers are usually delivered to combustion chambers as a spray of droplets, which then undergo a sequence of vaporization, mixing, ignition, and combustion processes at pressure levels well above the thermodynamic critical points of the fluids. Under these conditions, liquids initially injected at subcritical temperature may heat up and experience a thermodynamic state transition into the supercritical regime during their lifetimes. The process exhibits many characteristics distinct from those in an atmospheric environment, thereby rendering conventional approaches developed for low-pressure applications invalid.

Modeling supercritical mixing and combustion processes numerically poses a variety of challenges that include all of the classical closure problems and a unique set of problems imposed by the introduction of thermodynamic nonidealities and transport anomalies. From the classical point of view, reacting, multiphase flows introduce the complicating factors of chemical kinetics, highly nonlinear source terms, and a variety of sub-grid scale (SGS) velocity and

scalar-mixing interactions. Flowfield evolution is affected by compressibility effects (volumetric changes induced by changes in pressure) and variable inertia effects (volumetric changes induced by variable composition and/or heat addition). The resultant coupling dynamics yield an array of physiochemical processes that are dominated by widely disparate time and length scales, many being smaller than can be resolved in a numerically feasible manner. The situation becomes more complex with increasing pressure because of an inherent increase in the flow Reynolds number, which causes a further decrease in the scales associated with SGS interactions and difficulties that arise when fluid states approach the critical conditions. Near the critical point, propellant mixture properties exhibit liquid-like densities, gas-like diffusivities, and pressure-dependent solubilities. Surface tension and enthalpy of vaporization approach zero, and the isothermal compressibility and specific heat increase significantly. These phenomena, coupled with extreme local property variations, have a significant impact on the evolutionary dynamics exhibited by a given system.

This paper attempts to provide an overview of recent advances in theoretical modeling and numerical simulation of supercritical vaporization, mixing, and combustion processes in liquid-fueled propulsion systems. Three subject areas are considered: (1) droplet gasification and combustion, (2) spray field dynamics, and (3) multiphase mixing and combustion processes. A variety of liquid propellants and

propellant simulants, including hydrocarbon and cryogenic fluids, at both steady and oscillatory conditions, are treated systematically.

Supercritical Droplet Vaporization and Combustion

We first consider the vaporization and combustion of an isolated liquid droplet when suddenly placed in a combustion chamber. This configuration allows us to focus on the effects of pressure on the thermodynamic and transport processes involved. As a result of heat transfer from the surrounding gases, the droplet starts to heat up and evaporate due to the vapor concentration gradient near the surface. Two scenarios, subcritical and supercritical conditions, must be considered in order to provide a complete description of various situations encountered. If the chamber condition is in the thermodynamic subcritical regime of the injected liquid, the droplet surface provides a well-defined interfacial boundary. To facilitate analysis, physical processes in the droplet interior and ambient gases are treated separately and then matched at the interface by requiring liquid-vapor phase equilibrium and continuities of mass and energy fluxes. This procedure eventually determines the droplet surface conditions and evaporation rate. The situation, however, becomes qualitatively different in the supercritical regime. Then, the droplet may continuously heat up, with its surface reaching the critical mixing point prior to the end of the droplet lifetime. When this occurs, the sharp distinction between gas and liquid disappears. The enthalpy of vaporization reduces to zero, and no abrupt phase change is involved in the vaporization process. The density and temperature of the entire field as well as their gradients vary continuously across the droplet surface. The droplet interior, however, remains at the liquid state with a subcritical temperature distribution. For convenience of discussion, the droplet regression is best characterized by the motion of the surface which attains the critical mixing temperature of the system. The process becomes totally diffusion controlled.

Attempts to study supercritical droplet vaporization and combustion have been made for more than four decades. The earliest development of a predictive model was initiated by Spalding [1] and subsequently refined by Rosner [2]. Both studies considered an isolated fuel droplet in a stagnant environment by approximating the droplet as a point source of dense gas with constant physical properties. The same problem was re-examined by other researchers [3–5] in order to investigate the influence of convection, density variation, and finite rate chemical kinetics.

Systematic treatment of droplet vaporization at near-critical conditions was initiated by Manrique

and Borman [6], based on a quasi-steady model. They concluded that the effects of thermodynamic nonidealities, property variations, and high-pressure corrections for phase equilibrium modify the vaporization mechanisms significantly. In light of these findings, Lazar and Faeth [7] and Canada and Faeth [8] conducted a series of experimental and theoretical studies on droplet combustion in both stagnant and forced convective environments, with special attention focused on the high-pressure phenomena of phase equilibrium. The effects of forced convection in the gas phase were treated by conventional multiplicative corrections. The assumptions of quasi-steadiness and uniform property distributions adopted in Refs. [6–8] were later relaxed. In works by Rosner and Chang [9] and Kadota and Hiroyasu [10], the effects of transient processes, natural convection, and the conditions under which a droplet may be driven to its critical point were examined.

More recently, several researchers [11–17] have employed numerical techniques to simulate high-pressure droplet vaporization and combustion with considerable success. All of these models, however, adopted certain rudimentary assumptions and empirical formulas for fluid properties that were extrapolated from low-pressure cases, with their accuracy for high-pressure applications subject to question. Furthermore, no effort was made to treat the thermodynamic phase transition through the critical point. In order to remedy these deficiencies, a series of fundamental studies [18–28] were conducted using state-of-the-art treatment of thermodynamic and transport phenomena. Of particular importance is the unified analyses of thermophysical properties employed in Refs. [19–20] and [25–28] based on fundamental thermodynamic theories. These approaches allow for a self-consistent solution from first principles, thereby enabling a systematic investigation into underlying mechanisms involved in supercritical droplet gasification and combustion. The effect of non-equilibrium phase transition on droplet behavior was further addressed by Harstad and Bellan [25–28] using Keizer's fluctuation theory. In addition, Umemura and Shimada [29–31] constructed approximate analyses to elucidate many intriguing characteristics of supercritical droplet gasification. Extensive reviews of this subject were recently given Givler and Abraham [32] and Bellan [33].

Thermodynamic and Transport Properties

Owing to the continuous variations of fluid properties in supercritical environments, classical techniques dealing with liquids and gases individually often lead to erroneous results of droplet dynamics. The problem becomes even more exacerbated when the droplet surface approaches the critical condition.

The thermophysical properties usually exhibit anomalous variations and are very sensitive to both temperature and pressure in the vicinity of the critical point, a phenomenon commonly referred to as near-critical enhancement. Thus, an essential prerequisite of any realistic treatment of supercritical droplet behavior is the establishment of a unified property evaluation scheme capable of treating thermophysical properties of the system and its constituent species over the entire fluid thermodynamic state, from compressed liquid to dilute gas.

All the thermodynamic properties can be derived from a modified Benedict–Webb–Rubin (BWR) equation of state proposed by Jacobsen and Stewart [34] due to its superior performance over conventional cubic equations of state [35]. This equation of state has been extremely valuable in correlating both liquid and vapor thermodynamic and volumetric data; however, the temperature constants involved are available only for a limited number of pure substances [36]. To overcome this constraint, an extended corresponding-state (ECS) principle [37,38] is used. The basic idea is to assume that the properties of a single-phase fluid can be evaluated via conformal mappings of temperature and density to those of a given reference fluid. As a result, only the BWR constants for the reference fluid are needed. For a multicomponent system, accounting for changes in properties due to mixing is much more complicated. A pseudo pure-substance model is adopted to evaluate the properties of a mixture, treating the mixture as a single-phase pure substance with its own set of properties evaluated via the ECS principle. This method improves prediction accuracy and requires only limited data (i.e., critical properties and Pitzer’s acentric factor) for each constituent component.

Successful application of the corresponding-state argument for the evaluation of fluid p–V–T properties also encourages similar improvement in the prediction of thermophysical data. In the following, a brief summary of the corresponding-state method in conjunction with the mixture combining rule is first given, followed by the BWR equation of state for the reference fluid. Finally, the techniques for evaluating thermodynamic and transport properties are addressed.

Extended corresponding-state principle

The ECS model of Ely and Hanley [37,38] is used to evaluate volumetric and transport properties of a mixture over its entire thermodynamic fluid state. The scheme assumes that the configurational properties (such as temperature, density, viscosity, thermal conductivity, etc.) of a single-phase mixture can be equated to those of a hypothetical pure fluid, which are then evaluated via corresponding-state principles with respect to a given reference fluid. For example, the viscosity of a mixture, μ_m , can be

related to that of a reference fluid, μ_0 , at the corresponding thermodynamic state as

$$\mu_m(\rho, T) = \mu_0(\rho_0, T_0) F_\mu \quad (1)$$

where F_μ represents the mapping function. The correspondence of temperature and density between the mixture of interest and the reference fluid can be characterized by the following two scaling factors:

$$f_m = \frac{T}{T_0}; \quad \tilde{h}_m = \frac{\rho_0}{\rho} \quad (2)$$

The former represents the conformation of potential distribution of energy, while the latter characterizes the effect of mixture molecular size.

Equation of state

Under the assumption of the ECS principle, the density of a mixture can be evaluated by

$$\rho_m(T, p) = \frac{\rho_0(T_0, p_0)}{\tilde{h}_m(T, p)} \quad (3)$$

where ρ_0 , T_0 , and p_0 denote the corresponding density, temperature, and pressure of the reference fluid, respectively. Since the temperature at the conformal state is calculated by equation 2, the corresponding pressure can be derived based on the general compressibility theory:

$$p_0 = p \left(\frac{\tilde{h}_m}{f_m} \right) \quad (4)$$

To ensure the accuracy of the density prediction, a generalized BWR equation of state [34] is adopted for the reference fluid:

$$p_0(T, \rho) = \sum_{n=1}^9 a_n(T) \rho^n + \sum_{n=10}^{15} a_n(T) \rho^{2n-17} e^{-\gamma \rho^2} \quad (5)$$

where γ is 0.04, and the temperature coefficients $a_i(T)$ depend on the reference fluid used.

Although this equation of state must be solved iteratively for density at given pressure and temperature, the prediction covers a wide range of thermodynamic states and as such promotes the establishment of a unified evaluation scheme of thermophysical properties. Fig. 1 shows the comparison of oxygen density between experimental data [39] and the prediction by the BWR equation of state in conjunction with the ECS principle. The reference fluid is selected to be propane due to the availability of sufficiently reliable data correlated over a wide range of experimental conditions for this substance. The result shows excellent agreement over the entire fluid state. Fig. 2 presents the relative errors of density prediction based on three commonly used equations of state, namely, BWR, Peng–Robinson (PR),

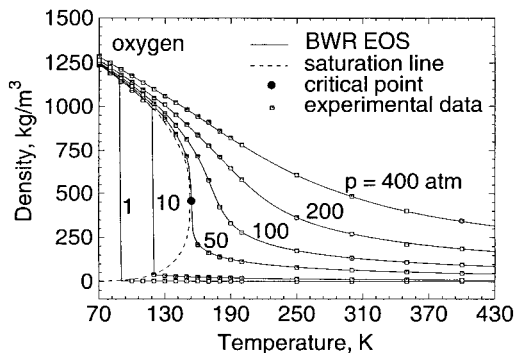


FIG. 1. Comparison of oxygen density predicted by the BWR equation of state and measured by Sychev et al. [39].

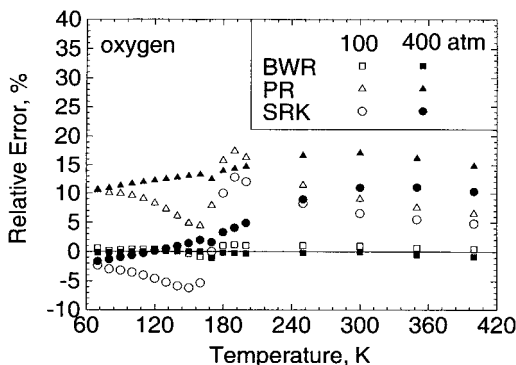


FIG. 2. Relative errors of density predictions by three different equations of state. Experimental data from Sychev et al. [39].

and Soave–Redlich–Kwong (SRK). The ECS principle is embedded into the evaluation procedure of the BWR equation of state and shows its superior performance with the maximum relative error of 1.5% for the pressure and temperature ranges under consideration. On the other hand, the SRK and PR equations of state yield maximum errors around 13% and 17%, respectively.

Thermodynamic Properties

Thermodynamic properties such as enthalpy, internal energy, and specific heat can be expressed as the sum of ideal-gas properties at the same temperature and departure functions which take into account the dense-fluid correction. Thus,

$$h = h^0 + \left\{ \int_{\infty}^v \left[T \left(\frac{\partial p}{\partial T} \right)_v - p \right] dv + RT(Z - 1) \right\} \quad (6)$$

$$e = e^0 + \left\{ \int_{\infty}^v \left[T \left(\frac{\partial p}{\partial T} \right)_v - p \right] dv \right\} \quad (7)$$

$$C_p = C_p^0 + \left\{ \int_{\infty}^v T \left(\frac{\partial^2 p}{\partial T^2} \right)_v dv - T \left(\frac{\partial p}{\partial T} \right)_v^2 / \left(\frac{\partial p}{\partial v} \right)_T - R \right\} \quad (8)$$

where superscripts 0 refer to ideal-gas properties. The second terms on the right sides of equations 6–8 denote the thermodynamic departure functions and can be obtained from the equation of state described previously.

Transport Properties

Estimation of viscosity and thermal conductivity can be made by means of the ECS principle. The corresponding-state argument for the viscosity of a mixture can be written in its most general form as

$$\mu_m(\rho, T) = \mu_0(\rho_0, T_0) F_{\mu} \chi_{\mu} \quad (9)$$

where F_{μ} is the scaling factor. The correction factor χ_{μ} accounts for the effect of non-correspondence and has the magnitude always close to unity based on the modified Enskog theory [40].

Because of the lack of a complete molecular theory for describing transport properties over a broad regime of fluid phases, it is generally accepted that viscosity and thermal conductivity can be divided into three contributions and correlated in terms of density and temperature [41]. For instance, the viscosity of the reference fluid is written as follows:

$$\mu_0(\rho_0, T_0) = \mu_0^0(T_0) + \Delta\mu_0^{\text{exc}}(\rho_0, T_0) + \Delta\mu_0^{\text{crit}}(\rho_0, T_0) \quad (10)$$

The first term on the right-hand side represents the value at the dilute-gas limit, which is independent of density and can be accurately predicted by kinetic-theory equations. The second term is the excess viscosity which, with the exclusion of unusual variations near the critical point, characterizes the deviation from μ_0 for a dense fluid. The third term refers to the critical enhancement which accounts for the anomalous increase above the background viscosity (i.e., the sum of μ_0^0 and $\Delta\mu_0^{\text{exc}}$) as the critical point is approached. However, the theory of nonclassical critical behavior predicts that, in general, properties that diverge strongly in pure fluids near the critical points diverge only weakly in mixtures due to the different physical criteria for criticality in a pure fluid and a mixture [42]. Because the effect of critical enhancement is not well-defined for a mixture and is likely to be small, the third term $\Delta\mu_0^{\text{crit}}$ is usually not considered in the existing analyses of supercritical droplet gasification.

Evaluation of thermal conductivity must be carefully conducted for two reasons: (1) the one-fluid model must ignore the contribution of diffusion to conductivity, and (2) the effect of internal degrees

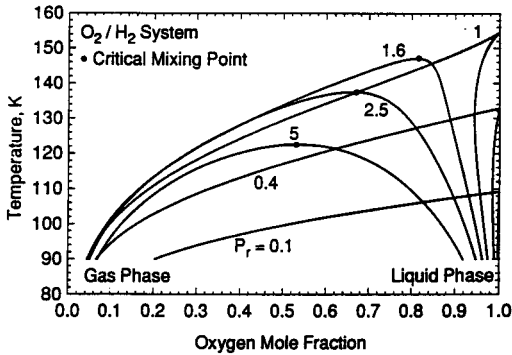


FIG. 3. Vapor-liquid phase equilibrium compositions for O₂/H₂ system at various pressures.

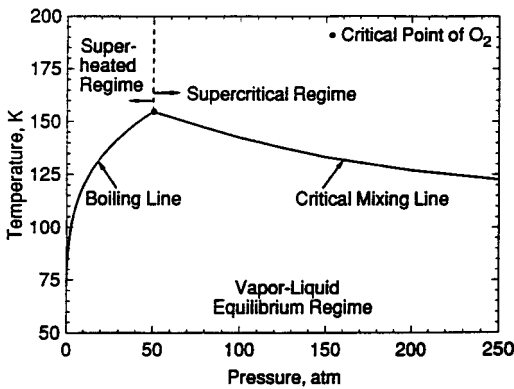


FIG. 4. Pressure-temperature diagram for phase behavior of O₂/H₂ system in equilibrium.

of freedom on thermal conductivity cannot be correctly taken into account by the corresponding-state argument. As a result, thermal conductivity of a pure substance or mixture is generally divided into two contributions [38]:

$$\lambda_m(\rho, T) = \lambda'_m(T) + \lambda''_m(\rho, T) \quad (10)$$

The former, $\lambda'_m(T)$, arises from transfer of energy via the internal degrees of freedom, while the latter, $\lambda''_m(\rho, T)$, is due to the effects of molecular collision or translation which can be evaluated by means of the ECS method. For a mixture, $\lambda'_m(T)$ can be evaluated by a semi-empirical mixing rule.

Estimation of the binary mass diffusivity for a mixture gas at high density represents a more challenging task than evaluating the other transport properties, due to the lack of a formal theory or even a theoretically based correlation. Takahashi [43] suggested a simple scheme for predicting the binary mass diffusivity of a dense fluid by means of a corresponding-state approach. The approach appears to be the most complete to date and has demonstrated

moderate success in the limited number of tests conducted. The scheme proceeds in two steps. First, the binary mass diffusivity of a dilute gas is obtained using the Chapman-Enskog theory in conjunction with the intermolecular potential function. The calculated data is then corrected in accordance with a generalized chart in terms of reduced temperature and pressure.

Vapor-Liquid Phase Equilibrium

The result of vapor-liquid phase equilibrium is required to specify the droplet surface behavior prior to the occurrence of critical conditions. The analysis usually consists of two steps. First, an appropriate equation of state as described in the section on thermodynamic and transport properties is employed to calculate fugacities of each constituent species in both gas and liquid phases. The second step lies in the determination of the phase equilibrium conditions by requiring equal fugacities for both phases of each species. Specific outputs from this analysis include (1) enthalpy of vaporization, (2) solubility of ambient gases in the liquid phase, (3) species concentrations at the droplet surface, and (4) conditions for criticality. The analysis can be further used in conjunction with the property evaluation scheme to determine other important properties such as surface tension.

As an example, the equilibrium compositions for a binary mixture of oxygen and hydrogen is shown in Fig. 3, where p_r represents the reduced pressure of oxygen. In the subcritical regime, the amount of hydrogen dissolved in the liquid oxygen is quite limited, decreasing progressively with increasing temperature and reducing to zero at the boiling point of oxygen. At supercritical pressures, however, the hydrogen gas solubility becomes substantial and increases with temperature. Because of the distinct differences in thermophysical properties between the two species, the dissolved hydrogen may appreciably modify the liquid properties and, subsequently, the vaporization behavior. The phase equilibrium results also indicate that the critical mixing temperature decreases with pressure.

The overall phase behavior in equilibrium is best summarized by the pressure-temperature diagram in Fig. 4, which shows how the phase transition occurs under different thermodynamic conditions. The boiling line is made up of boiling points for subcritical pressure. As the temperature increases, an equilibrium vapor-liquid mixture may transit to superheated vapor across this line. The critical mixing line registers the variation of the critical mixing temperature with pressure. It intersects the boiling line at the critical point of pure oxygen, the highest temperature at which the vapor and liquid phases of an O₂/H₂ binary system can coexist in equilibrium.

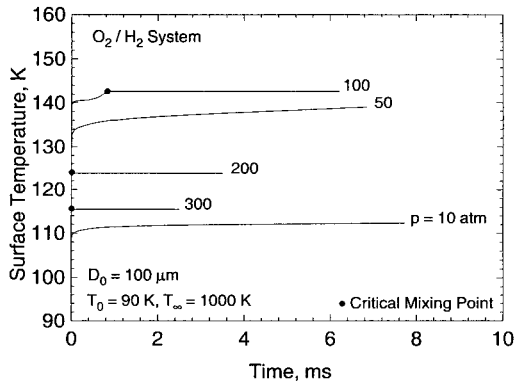


FIG. 5. Time variations of droplet surface temperature at various pressures. $T_\infty = 1000$ K, $T_0 = 90$ K, $D_0 = 100$ μm .

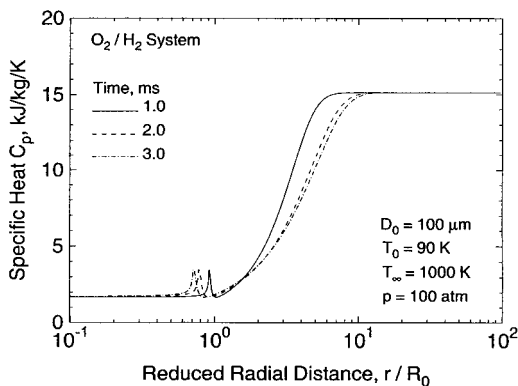


FIG. 6. Instantaneous distributions of mixture specific heat in the entire field at various times. $T_0 = 90$ K, $T_\infty = 1000$ K, $p = 100$ atm, $D_0 = 100$ μm .

Droplet Vaporization in Quiescent Environments

Several theoretical works have recently been devoted to the understanding of droplet vaporization and combustion under high-pressure conditions. Both hydrocarbon droplets in air [11–13,18,27,28] and liquid oxygen (LOX) droplets in hydrogen [14,17,19–26,44] were treated comprehensively, with emphasis placed on the effects of transient diffusion and interfacial thermodynamics. The works of Lafon et al. [22,44], Hsiao and Yang [20,45], and Harstad and Bellan [25–28] appear to be the most complete to date because of the employment of a unified property evaluation scheme, as outlined previously.

We first consider the vaporization of LOX droplet in either pure hydrogen or mixed hydrogen/water environments [22,44] due to its broad applications in cryogenic rocket engines using hydrogen and oxygen as propellants [46]. Fig. 5 shows the time variations of droplet surface temperature at various

pressures. The ambient hydrogen temperature is 1000 K. Three different scenarios are noted. First, at low pressures (i.e., $p = 10$ atm), the surface temperature rises suddenly and levels off at the pseudo wet-bulb state, which is slightly lower than the oxygen boiling temperature because of the presence of hydrogen on the gaseous side of the interface. For higher pressures (i.e., $p = 50$ atm), the surface temperature rises continuously. The pseudo wet-bulb state disappears, and the vaporization process becomes transient in nature during the entire droplet lifetime. For $p = 100$ atm, the droplet surface even reaches its critical state at 1 ms. Fig. 6 shows the distributions of the mixture specific heat at various times. The weak divergence of the specific heat near the droplet surface (i.e., defined as the surface attaining the critical-mixing temperature) is clearly observed.

An extensive series of numerical simulations were conducted for a broad range of ambient temperatures ($500 \leq T_\infty \leq 2500$ K) and pressures up to 300 atm. The calculated LOX droplet lifetime in pure hydrogen can be well correlated using an approximate analysis that takes into account the effect of transient heat diffusion in terms of the reduced critical temperature, $T_c^* = (T_\infty - T_c)/(T_\infty - T_0)$. The resultant expression of the droplet lifetime takes the form

$$\tau = [0.0115 + 0.542(1 - T_c^*)] \frac{R_0^2}{\alpha_0^2} f(\alpha_\infty/\alpha_0^1) \quad (11)$$

where the correction factor is chosen as

$$f(\alpha_\infty/\alpha_0^1) = 1 + 3.9[1 - \exp(-0.035(\alpha_\infty/\alpha_0^1 - 1))] \quad (12)$$

The expression of T_c^* may be related to the Spalding transfer number, which has more physical significance, as follows:

$$B_T = \frac{T_\infty - T_c}{T_c - T_0} = \frac{T_c^*}{1 - T_c^*} \quad (13)$$

This correlation clearly shows that pressure affects the droplet lifetime through its influence on the mixture critical temperature and ambient thermal diffusivity.

The behavior of hydrocarbon fuel droplets basically follow the same trend as cryogenic droplets in terms of their vaporization characteristics. In general, the droplet lifetime decreases smoothly with increasing pressure, and no discernible variation occurs across the critical transition. In the subcritical regime, the decrease in enthalpy of vaporization with pressure facilitates vaporization process and consequently leads to a decrease in droplet lifetime. The situation becomes different at supercritical conditions, at which the interfacial boundary disappears

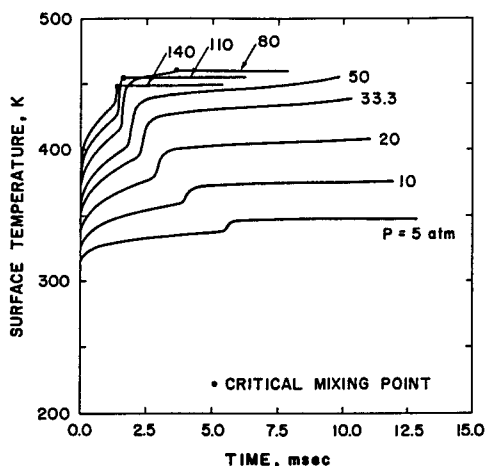


FIG. 7. Time variations of droplet surface temperature at various pressures, *n*-pentane/air system.

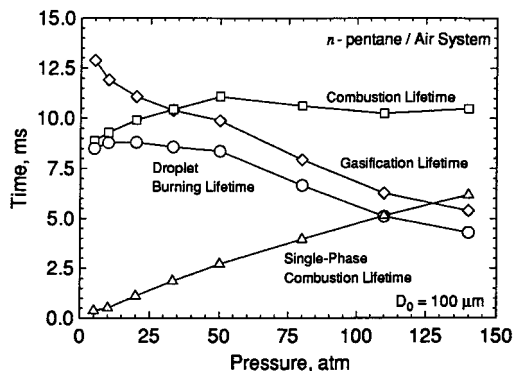


FIG. 8. Effect of pressure on milestone times associated with droplet gasification and burning processes, *n*-pentane/air system. $T_0 = 300$ K, $T_\infty = 1000$ K.

with the enthalpy of vaporization being zero. In this case, the decrease in droplet lifetime is mainly attributed to the increase in thermal diffusivity near the droplet surface. As critical conditions are approached, the divergence of the specific heat compensates for the effect of vaporization enthalpy reduction, so that no abrupt change occurs during the critical transition.

Droplet Combustion in Quiescent Environments

Much effort was devoted to the study of supercritical droplet combustion (e.g., Refs. [17,18,22]). In spite of the presence of chemical reactions in the gas phase, the general characteristics of a burning droplet are similar to those involving only vaporization. We consider here the combustion of a hydrocarbon (e.g., *n*-pentane) fuel droplet in air [18]. The

droplet initial temperature is 300 K, and the ambient air temperature is 1000 K. Fig. 7 shows the time history of the droplet surface temperature at various pressures for $D_0 = 100 \mu\text{m}$. Once ignition is achieved in the gas phase, energy feedback from the flame causes a rapid increase in droplet surface temperature. At low pressures ($p \leq 20$ atm), the surface temperature varies very slowly following onset of flame development and almost levels off at the pseudo wet-bulb state. As the ambient pressure increases, the high concentrations of oxygen in the gas phase and the fuel vapor issued from the droplet surface result in a high chemical reaction rate, consequently causing a progressive decrease in ignition time. Furthermore, the surface temperature jump during the flame-development stage increases with increasing pressure. Since the critical mixing temperature decreases with pressure, the droplet reaches its critical condition more easily at higher pressures, almost immediately following establishment of the diffusion flame in the gas phase for $p \geq 110$ atm.

Figure 8 presents the effect of pressure on various milestone times associated with droplet gasification and burning process for $D_0 = 100 \mu\text{m}$ [18]. Here, gasification lifetime is the time required for complete gasification; droplet burning lifetime is the gasification lifetime minus ignition time; single-phase combustion lifetime is the time duration from complete gasification to burnout of all fuel vapor; combustion lifetime is the sum of single-phase combustion lifetime and droplet burning lifetime. The gasification lifetime decreases continuously with pressure, whereas the single-phase combustion lifetime increases progressively with pressure due to its adverse effect on mass diffusion. More importantly, the pressure dependence of combustion lifetime exhibits irregular behavior. This phenomenon may be attributed to the overlapping effect of reduced enthalpy of vaporization and mass diffusion with increasing pressure.

Since the time scales for diffusion processes are inversely proportional to the droplet diameter squared, it is important to examine the effect of droplet size on the burning characteristics. In this regard, calculations were conducted for large droplets having an initial diameter of $1000 \mu\text{m}$, which is comparable to the sizes considered in most experimental studies of supercritical droplet combustion [47–49]. Furthermore, the ignition transient occupies only a small fraction of the entire droplet lifetime for large droplets. The uncertainties associated with the ignition procedure in determining the characteristics of droplet gasification can be minimized. Consequently, a more meaningful comparison with experimental data can be made. The combustion behavior of a large droplet reveals several characteristics distinct from those of a small droplet. First, ignition for large droplets occurs in the very early stage

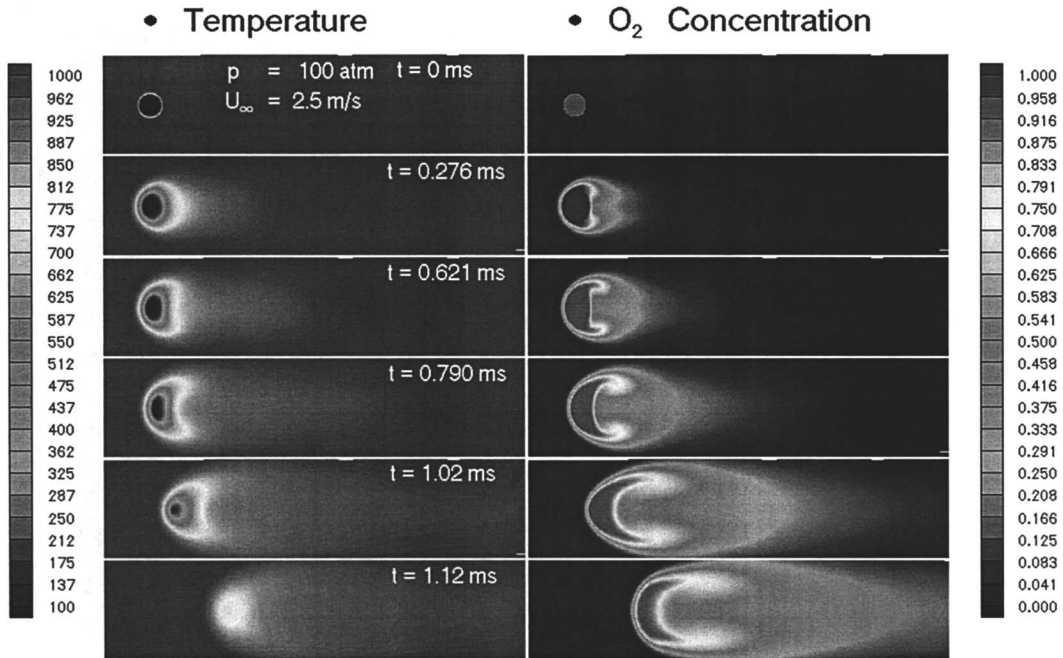


FIG. 9. LOX droplet gasification in supercritical hydrogen flow. $p = 100$ atm, $U_\infty = 2.5$ m/s.

of the entire droplet lifetime. The influence of gasification prior to ignition on the overall burning mechanisms appears to be quite limited. Second, the combustion lifetime decreases with increasing pressure, reaching a minimum near the critical pressure of the liquid fuel. As the pressure further increases, the combustion time increases due to reduced mass diffusivity at high pressures. The gasification lifetime decreases continuously with pressure, whereas the single-phase combustion lifetime increases progressively with pressure. At low pressures, the gasification of liquid fuel primarily controls the combustion process, whereas in a supercritical environment, the transient gas-phase diffusion plays a more important role.

Droplet Vaporization in Convective Environments

When a droplet is introduced into a cross-flow, the forced convection results in increases of heat and mass transfer between the droplet and surrounding gases, which consequently intensifies the gasification process. Although many studies have been conducted to examine droplet vaporization in forced-convective environments, effects of pressure and freestream velocities on droplet dynamics, especially for rocket engine applications which involve supercritical conditions, have not yet been addressed in detail. Hsiao et al. [20,45] developed a comprehensive analysis of LOX droplet vaporization in a supercritical hydrogen stream, covering a pressure range

of 100–400 atm. The model takes into account multidimensional flow motions and enables a thorough examination of droplet behavior during its entire lifetime, including dynamic deformation, viscous stripping, and secondary breakup. Detailed flow structures and thermodynamic properties are obtained to reveal mechanisms underlying droplet gasification as well as deformation and breakup dynamics.

Figure 9 shows six frames of isotherms and isopleths of oxygen concentration at a convective velocity of 2.5 m/s and an ambient pressure of 100 atm. The freestream Reynolds number Re is 31, based on the initial droplet diameter. Soon after the introduction of the droplet into the hydrogen stream, the flow adjusts to form a boundary layer near the surface. The gasified oxygen is carried downstream through convection and mass diffusion. The evolution of the temperature field exhibits features distinct from that of the concentration field due to the disparate time scales associated with thermal and mass diffusion processes (i.e., Lewis number $\neq 1$). The thermal wave penetrates into the droplet interior with a pace faster than does the surrounding hydrogen species. Since the liquid core possesses large momentum inertia and moves slower compared with the gasified oxygen, at $t = 0.79$ ms, the droplet (delineated by the dark region in the temperature contours) reveals an olive shape, while the oxygen concentration contours deform into a crescent shape with the edge bent to the streamwise direction. At $t = 1.08$ ms, the subcritical liquid core

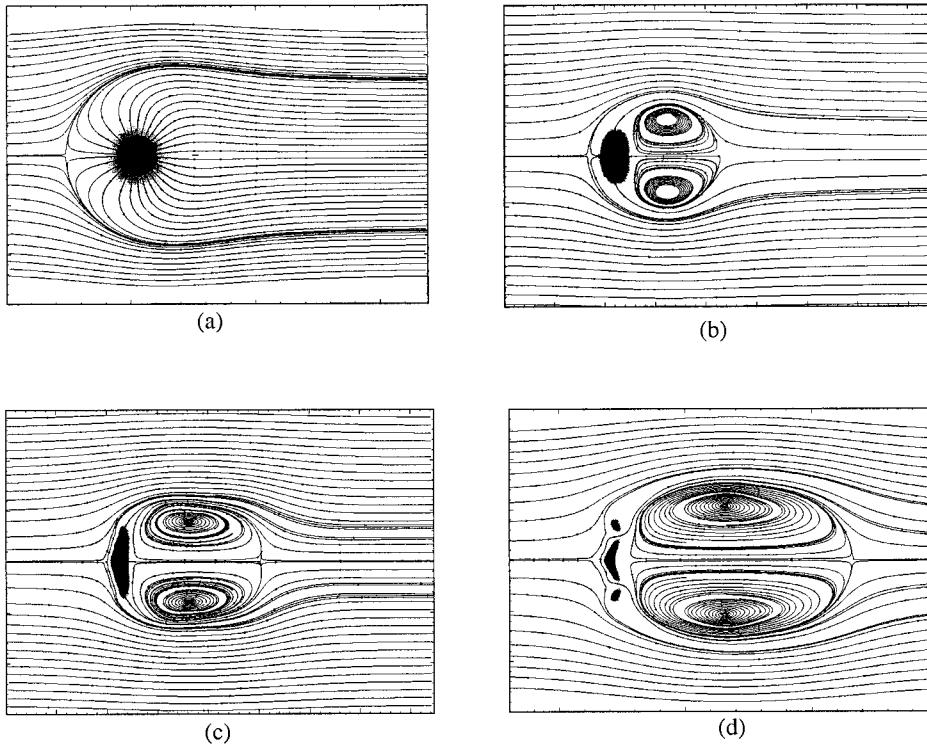


FIG. 10. LOX droplet gasification in supercritical hydrogen flow at $p = 100$ atm. (a) Spherical mode. $U_\infty = 0.2$ m/s, $t = 0.61$ ms. (b) Deformation mode. $U_\infty = 1.5$ m/s, $t = 0.61$ ms. (c) Stripping mode. $U_\infty = 5$ m/s, $t = 0.17$ ms. (d) Breakup mode. $U_\infty = 15$ m/s, $t = 0.17$ ms.

disappears, leaving behind a puff of dense oxygen fluid which is convected further downstream with increasing velocity until it reaches the momentum equilibrium with the ambient hydrogen flow.

Figure 10 summarizes the streamline patterns and oxygen concentration contours of the four different modes commonly observed in supercritical droplet gasification. The droplet may either remain in a spherical configuration, deform to an olive shape, or even break up into fragments, depending on the local flow conditions. Unlike low-pressure cases in which the large shear stress at the gas-liquid interface induces internal flow circulation in the liquid core [50], no discernible recirculation takes place in the droplet interior, regardless of the Reynolds number and deformation mode. This may be attributed to the diminishment of surface tension at supercritical conditions. In addition, the droplet regresses so fast that a fluid element in the interphase region may not acquire the time sufficient for establishing an internal vortical flow before it gasifies. The rapid deformation of the droplet configuration further precludes the existence of stable shear stress in the liquid core and consequently obstructs the formation of recirculation.

The spherical mode shown in Fig. 10a typically occurs at very low Reynolds numbers. Although flow separation is encouraged by LOX gasification, no recirculating eddy is found in the wake behind the droplet. The vorticity generated is too weak to form any confined eddy. When the ambient velocity increases to 1.5 m/s, the droplet deforms into an olive shape with a recirculating ring attached behind it, as shown in Fig. 10b. Owing to the droplet deformation and gasification, the threshold Reynolds number above which the recirculating eddy forms is considerably lower than that for a hard sphere. Figure 10c depicts the flow structure with viscous stripping at an ambient velocity of 5 m/s, showing an oblate droplet with a stretched vortex ring. The flattened edge of the droplet enhances the strength of the recirculating eddies and as such increases the viscous shear stress dramatically. Consequently, a thin sheet of fluid is stripped off from the edge of the droplet and swept toward the outer boundary of the recirculating eddy. At a very high ambient velocity of 15 m/s, droplet breakup takes place, as clearly shown in Fig. 10d. The hydrogen flow penetrates through the liquid phase and divides the droplet into two

parts: the core disk and surrounding ring. The vortical structure in the wake region expands substantially as a result of the strong shear stress.

The effect of ambient pressure and Reynolds number on droplet lifetime can be correlated with respect to the reference value at zero Reynolds number. The result takes the form

$$\frac{\tau_f}{\tau_{f, Re=0}} = \frac{1}{1 + 0.17Re^{1.1}(p_{r,O_2})^{-0.88}} \quad (14)$$

where Re and p_{r,O_2} refer to the Reynolds number based on the initial droplet diameter and the reduced pressure of oxygen, respectively. This correlation bears a resemblance to the popular Ranz-and-Marshall correlation [51] for droplet heat-transfer correction due to convective effect. The Ranz-and-Marshall correlation applies only to low pressure flows and has a weaker Reynolds number dependency.

Drag coefficient has been generally adopted as a dimensionless parameter to measure the drag force acting on a droplet. Chen and Yuen [52] found that the drag coefficient of an evaporating droplet is smaller than that of a non-vaporizing solid sphere at the same Reynolds number. Several researchers [53,54] numerically analyzed evaporating droplet motion by solving the Navier–Stokes equations and proposed the following correlation:

$$C_D = \frac{C_D^0}{(1 + B)^b} \quad (15)$$

where C_D^0 denotes the drag coefficient for a hard sphere, and b is a constant which has a value of 0.2 for Reksizbulut's model and 0.32 for Chiang's correlation. A transfer number B is adopted to account for the effect of blowing on momentum transfer to the droplet. For droplet vaporization at low to moderate pressures ($p_r \leq 0.5$), the Spalding transfer number is widely used to characterize the vaporization rate:

$$B = \frac{C_p(T_\infty - T_s)}{\Delta h_v} \quad (16)$$

The enthalpy of vaporization Δh_v becomes zero at the critical point, rendering an infinite value for the transfer number. This deficiency may be remedied by introducing a transfer number suited for supercritical droplet vaporization [20,45].

$$B_D = \left(\frac{T_\infty - T_c}{T_c - T_1} \right) \quad (17)$$

where T_1 is the instantaneous average temperature of droplet, and T_c the critical mixing temperature. Since B_D diverges at $T_c = T_1$ at the end of droplet lifetime, the calculation of drag force was terminated when $T_c = T_1$ becomes less than 1 K, at which the

droplet residual mass is usually less than one thousandth of the initial mass. The influence on the accuracy of data reduction is quite limited. Following the procedure leading to equation 15, a correlation for LOX droplet drag coefficient is obtained:

$$C_D = \frac{C_D^0}{(1 + aB_D)^b} \quad (18)$$

where a and b are selected to be 0.05 and 1.592 ($p_{r,O_2})^{-0.7}$, respectively. The data clusters along the classical drag curve (equation 15) in the low Reynolds-number region, but deviates considerably at high Reynolds numbers (i.e., $Re > 10$). Although a shape factor may be employed to account for this phenomenon arising from the increased form drag due to droplet deformation, the difficulty of calculating this factor and conducting the associated data analysis precludes its use in correlating the drag coefficient herein. Instead, a simple correction factor $Re^{0.3}$ is incorporated into equation 18 to provide the compensation. The final result is given below:

$$C_D = \frac{C_D^0 Re^{0.3}}{(1 + aB_D)^{1.592(p_{r,O_2})^{-0.7}}} \quad 0 < Re < 300 \quad (19)$$

Droplet Response to Ambient Flow Oscillation

Although unsteady droplet vaporization and combustion have long been recognized as a crucial mechanism for driving combustion instabilities in liquid-fueled propulsion systems [55], they are extremely difficult to measure experimentally. In particular, the measurement of the effect of transverse oscillations on instantaneous evaporation and/or burning rates is quite formidable. The droplet volume dilatation arising from rapid temperature increase may overshadow the surface regression associated with vaporization and thereby obscure the data analysis, especially in the early stage of the droplet lifetime. Furthermore, conventional suspended-droplet experiments may not be feasible in the presence of gravity due to reduced or diminished surface tension. In view of these difficulties, it is advantageous to rely on theoretical analyses to study the responses of droplet vaporization and combustion to ambient flow oscillations. The model is based on the general approach described in Refs. [20] and [44], but with a periodic pressure oscillation superimposed in the gas phase. Both cases involving hydrocarbon droplets in nitrogen [20] and LOX droplets in hydrogen [22] are examined carefully. The purpose of these studies is to assess the effect of flow oscillation on vaporization process as a function of frequency and amplitude of the imposed oscillation as well as its type.

The most significant result is the enhanced droplet vaporization response with increasing ambient mean pressure. Among the various factors contributing to

this phenomenon, the effect of pressure on enthalpy of vaporization plays a decisive role. At high pressures, the enthalpy of vaporization decreases substantially and becomes sensitive to variations of ambient pressure and temperature. Any small fluctuations in the surrounding gases may considerably modify the interfacial thermodynamics and consequently enhance the droplet vaporization response. This phenomenon is most profound when the droplet surface reaches its critical condition at which a rapid amplification of vaporization response function is observed. The enthalpy of vaporization and related thermophysical properties exhibit abnormal variations in the vicinity of the critical point, thereby causing a sudden increase in the vaporization response. On the other hand, the effect of mean pressure on the phase angle of response function appears quite limited. The phase angle decreases from zero at the low-frequency limit to -180° at high frequency, a phenomenon which can be easily explained by comparing various time scales associated with fluid transport and ambient disturbance.

Supercritical Spray Field Dynamics

Modeling high-pressure, multiphase combustion dynamics in a fully coupled manner poses a variety of challenges. In addition to the classical closure problems associated with turbulent reacting flows, the situation is compounded with increasing pressure due to the introduction of thermodynamic non-idealities and transport anomalies. A comprehensive discussion of this subject is given by Oefelein and Yang [56–58].

Experimental efforts to characterize propellant injection, mixing, and combustion processes at near- and super-critical conditions have only recently led to a better qualitative understanding of the mechanisms involved [59–65]. The current database, however, is not adequate with respect to quantitative assessments, and theoretical efforts are similarly deficient because of a lack of validated theories, difficulties associated with numerical robustness, and limited computational capacities. Depending on the injector type, fluid properties, and flow characteristics, two limiting extremes may be deduced [58]. At subcritical chamber pressures, injected liquid jets undergo the classical cascade of processes associated with atomization. For this situation, dynamic forces and surface tension promote the formation of a heterogeneous spray that evolves continuously over a wide range of thermophysical regimes. As a consequence, spray flames form and are lifted away from the injector face in a manner consistent with the combustion mechanisms exhibited by local droplet clusters. When chamber pressures approach or exceed the critical pressure of a particular propellant, however, injected liquid jets undergo a “transcritical”

change of state as interfacial fluid temperatures rise above the saturation or critical temperature of the local mixture. For this situation, diminished intermolecular forces promote diffusion-dominated processes prior to atomization and respective jets vaporize, forming a continuous fluid in the presence of exceedingly large gradients. Well-mixed diffusion flames evolve and are anchored by small but intensive recirculation zones generated by the shear layers imposed by adjacent propellant streams. These flames produce wakes that extend far downstream.

Figure 11, excerpted from Ref. 58, illustrates the basic phenomena just described for the case of a LOX/gaseous hydrogen shear-coaxial injector element. The optical diagnostic studies conducted by Mayer et al. [59,60] and Candel et al. [63,64] demonstrated the dramatic effect of pressure on mixing and combustion processes within this type of injector. When the liquid oxygen is injected at low-subcritical pressures, jet atomization occurs, forming a distinct spray similar to that depicted in Fig. 11a. Ligaments are detached from the jet surface, forming spherical droplets, which subsequently break up and vaporize. As the chamber pressure approaches the thermodynamic critical pressure of oxygen, the number of droplets present diminishes, and the situation depicted in Fig. 11b dominates. For this situation, thread-like structures evolve from the liquid core and diffuse rapidly within the shear layer induced by the co-flowing jets. At a downstream distance of approximately 50 diameters, the dense fluid core breaks into “lumps,” which are of the same order of magnitude as the diameter of the LOX jet. Results of optical measurements [59–64] reveal that flame attachment occurs instantaneously after ignition in the small but intensive recirculation zone that forms just downstream of the annular post. A well-mixed diffusion flame forms within this region, producing a wake that separates the oxygen stream from the hydrogen-rich outer flow. This wake persists at least 15 jet diameters downstream. Fig. 12 shows the resultant flame structure and corresponding flow-field. Here, the injected jet exhibits a pure diffusion mechanism at a pressure of 4.5 MPa, which is slightly below the thermodynamic critical pressure of oxygen, but significantly above that of hydrogen. Hutt and Cramer [66] have reported similar findings using a swirl-coaxial configuration.

The trends outlined in the preceding text coincide with the results of high-pressure liquid nitrogen/helium cold-flow tests reported in Refs. [60] and [65]. From a qualitative standpoint, these experiments have demonstrated the effect of mixture properties on injected liquid jets and the prevalence of one limit over the other, as illustrated in Fig. 11. The cutoff associated with these two limits, however, is not distinct and does not necessarily coincide with the critical point properties of either propellant. The

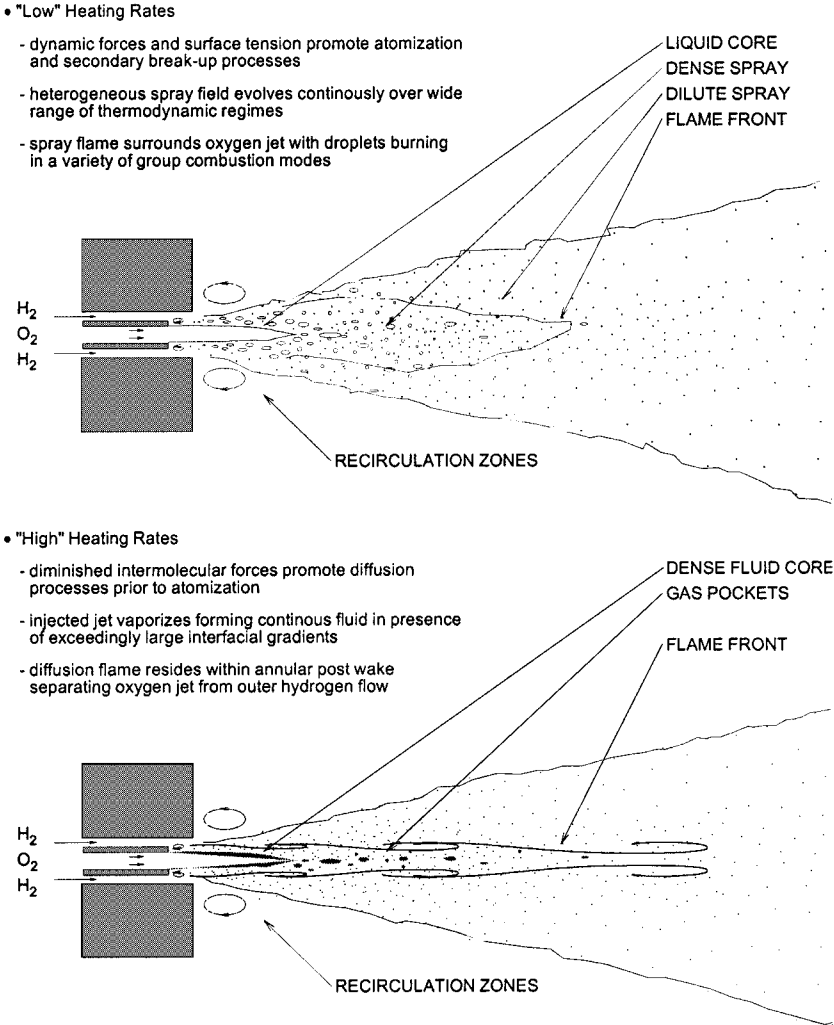


FIG. 11. Schematic diagram illustrating the basic phenomena associated with (top) low and (bottom) high chamber pressures for the case of a LOX/gaseous hydrogen shear-coaxial injector element [58].

dynamic forces associated with a swirl-coaxial injector, for example, would most likely dominate even under supercritical chamber conditions. For this situation, a combination of dense transcritical spray dynamics and diffusion-dominated processes would need to be considered. A shear-coaxial element, however, would be more prone to exhibit a pure diffusion mechanism. Transient conditions would alter the dynamics associated with either extreme. Thus, depending on the situation, a combination of two fundamental theoretical approaches is warranted [58]. The first is the classical Lagrangian–Eulerian implementation in which a particulate phase is assumed to exist in the flowfield. The second employs a pure Eulerian implementation to treat a dense

multicomponent fluid. Both approaches require detailed representations of mixture properties and microscale interactions over the full range of thermophysical regimes encountered in contemporary systems.

The complexity of the system outlined earlier is numerically demanding, and several tradeoffs are required with respect to the hierarchy of processes and characteristic scales resolved. A variety of uncertainties exist with regard to the closure problem, and in many cases computational capacity is in direct conflict with the accuracy of the SGS models employed. To address these difficulties in a manner consistent with current experimental efforts, Oefelein [56–58] focused on detailed representations of fluid dynamic

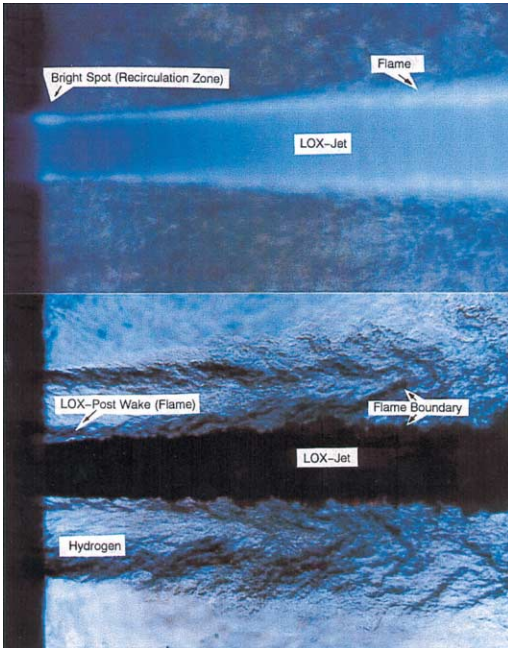


FIG. 12. Near injector region of a LOX/gaseous hydrogen shear-coaxial injector. (a) Flame. (b) Corresponding flowfield. Oxygen and hydrogen velocities are 30 and 300 m/s, respectively. Oxygen and hydrogen injection temperatures are 100 and 300 K. Oxygen jet diameter is 1 mm, and the chamber pressure is 4.5 MPa [59].

and physicochemical processes within planar mixing layers. The hydrogen/oxygen system is employed in all cases. The approach follows four fundamental steps: (1) development of a general theoretical framework, (2) specification of detailed property evaluation schemes and consistent closure methodologies, (3) implementation of an efficient and time-accurate numerical framework, and (4) simulation and analysis of a systematic series of case studies that focus on model performance and accuracy requirements.

The theoretical framework developed by Oefelein accommodates dense multicomponent fluids in the Eulerian frame and dilute particle dynamics in the Lagrangian frame over a wide range of scales in a fully coupled manner. This system is obtained by filtering the small-scale dynamics from the resolved scales over a defined set of spatial and temporal intervals. Beginning with the instantaneous system, filtering is performed in two stages. First, the influences of SGS turbulence and chemical interactions are taken into account, yielding the well-known closure problem for turbulent reacting gases. The second filtering operation incorporates SGS particle interactions. The resultant system of Favre-filtered conservation equations of mass, momentum, total

energy, and species concentration for a compressible, chemically reacting fluid composed of N species are derived.

Modeling SGS phenomena poses stringent numerical demands, and robust models are currently beyond the state of the art. Because of the uncertainties associated with the current models and the intensive numerical demands that these models place on computational resources, the current work neglects the effects of SGS scalar-mixing processes and focuses on detailed treatments of thermodynamic nonidealities and transport anomalies. To account for these effects over a wide range of pressure and temperature, the extended corresponding states principle outlined in the section on thermodynamic and transport properties is employed using two different equations of state. The 32-term BWR equation of state is used to predict the fluid pressure–volume–temperature (PVT) behavior in the vicinity of the critical point. The SRK equation of state is used elsewhere. Having established an analytical representation for the real mixture PVT behavior, explicit expressions for the enthalpy, Gibbs energy, and constant pressure specific heat are obtained as a function of temperature and pressure using Maxwell's relations to derive thermodynamic departure functions. Viscosity, thermal conductivity, and effective mass diffusion coefficients are obtained in a similar manner.

Turbulence quantities are modeled using the large-eddy simulation (LES) technique and the SGS models proposed in Ref. [67]. Spray dynamics are treated by solving a set of Lagrangian equations of motion and transport for the life histories of a statistically significant sample of particles. Here, the stochastic separated flow (SSF) methodology developed by Faeth [68] is employed, with transcritical droplet dynamics modeled using a set of correlations summarized previously.

The analyses developed were applied to study transcritical spray dynamics in a manner consistent with the phenomena depicted in Fig. 11a. Effort was first devoted to assessing the effect of pressure on thermophysical properties such as kinematic viscosity. This quantity is particularly significant and has a direct impact on the characteristic scales associated with the turbulence field. For both oxygen and hydrogen, an increase in pressure from 1 to 100 atm results in a corresponding reduction in the kinematic viscosity of up to three orders of magnitude. This implies a three order of magnitude increase in the characteristic Reynolds number. Based on Kolmogorov's universal equilibrium theory, the order of magnitude of the Kolmogorov microscale, denoted here as ν_t , and the Taylor microscale, λ_t , are related to the Reynolds number by equations of the form

$$\frac{\eta_t}{l_t} \sim Re_t^{-3/4}, \quad \frac{\lambda_t}{l_t} \sim Re_t^{-1/2} \quad (20)$$

Here, the Reynolds number is defined as $Re_t =$

$q_t l_t / \nu$, where $q_t = \sqrt{2k_t/3}$. The term q_t represents the turbulence intensity, k_t the SGS kinetic energy, and l_t the integral length scale. The relations given by equation 20 indicate that a three order of magnitude decrease in the kinematic viscosity results in 2.25 and 1.5 order of magnitude decreases in the Kolmogorov and Taylor microscales, respectively. These reductions have a direct impact on the overall grid density required to resolve key processes. The trend associated with the effective mass diffusivity is also of concern. When the pressure is increased from 1 to 100 atm, oxygen and hydrogen exhibit a two order of magnitude decrease in the mass diffusion rate over the full range of temperatures considered. Oxygen exhibits a decrease of up to four orders of magnitude at temperatures below the critical mixing point. The diminished mass diffusion rates coupled with the liquid-like densities at high pressures significantly alter the coupling dynamics associated with local fluid dynamic and physicochemical interactions.

A sequence of representative calculations were conducted which highlight dominate processes associated with high-pressure spray field dynamics in turbulent mixing layers [56–58]. In contrast to the low-pressure case, high-pressure mixing characteristics are much more sensitive to SGS fluctuations and the large-scale coherency associated with the gas phase. Gas-phase dynamics are also affected by the spray as a result of particle damping, transport between phases, and induced variations in mixture properties. Such changes alter the evolutionary structure of the flowfield. Momentum exchange between particles and the gas phase tends to damp the velocity field and reduce the level of turbulent diffusion. Elevated pressures, on the other hand, can significantly increase turbulent diffusion processes. Over the ranges considered, the change in density that accompanies increasing pressure causes the molecular kinematic viscosity to decrease significantly. This produces an overall increase in the local Reynolds number, and the normalized turbulent viscosity ratio. These effects amplify the dispersion attributes associated with the spray and markedly alter mixing and combustion processes at high pressures.

Supercritical Mixing and Combustion Processes

Extensive effort has been made by Oefelein and Yang [58] to study supercritical mixing and combustion of cryogenic propellants, motivated by the flow visualization experiments conducted by Mayer and Tamura [59–62] (see Fig. 12). Much insight was also achieved by Candel and his co-workers using laser-based optical diagnostic techniques [63,64]. Emphasis was placed on the near-field physicochemical processes that occur in the vicinity of the splitter plate,

the impact of pressure on these processes, and the downstream flow dynamics induced as a consequence. The computational domain consists of co-flowing hydrogen and oxygen streams separated by a 0.5 mm splitter plate, as shown in Fig. 13. A heat conduction model was applied to the splitter plate to provide a realistic energy flux distribution at the walls. Conditions were specified using a reference pressure of 100 atm, with the injection temperatures selected to produce an optimal matrix of transcritical and supercritical conditions.

Two sets of inlet flow conditions were examined at $p = 100$ atm, as detailed in Ref. [58]. The first set provides thermodynamic conditions similar to those employed by Mayer and Tamura [59]. Hydrogen and oxygen injection temperatures of $T_1 = 150$ K and $T_2 = 100$ K are specified to produce a supercritical hydrogen stream and a liquid oxygen stream that undergoes a transcritical change of state within the mixing layer. The corresponding oxygen to hydrogen density ratio is $\rho_2/\rho_1 = 72.7$. The second set of conditions provides supercritical states within both streams. For these cases hydrogen and oxygen injection temperatures of $T_1 = T_2 = 300$ K are specified to produce an oxygen to hydrogen density ratio of $\rho_2/\rho_1 = 17.4$.

Representative results are given in Figs. 14 and 15. Fig. 14 shows the instantaneous density and temperature fields for $U_1 = 125$ m/s and $U_2 = 30$ m/s. The corresponding plots for the supercritical case are presented in Fig. 15. The solutions shown provide a comparison between transcritical and supercritical mixing in the near field when respective hydrogen and oxygen streams are injected at identical velocities.

Transcritical mixing induces a vortical structure within the injected hydrogen stream that is analogous to that produced by a backward-facing step. This structure emanates from the upper corner of the splitter plate and coalesces downstream with adjacent vortices. The oxygen stream, on the other hand, exhibits no noticeable structure and proceeds unimpeded in an essentially straight line. Because of the liquid-like characteristics of the oxygen stream, an extremely large-density gradient exists within this region. Diminished mass diffusion rates are also evident. The combined effect produces a flame that behaves in a manner qualitatively similar to that depicted in Fig. 11. Combustion occurs at near stoichiometric conditions and produces a wake that effectively separates the hydrogen and oxygen streams as the flow evolves downstream.

A direct comparison between Figs. 14 and 15 highlights the wide disparities that exist between transcritical and supercritical fluid dynamic and physicochemical interactions. In contrast to the transcritical situation, relatively strong vortical interactions are prevalent between the oxygen and hydrogen streams at pure supercritical conditions. The

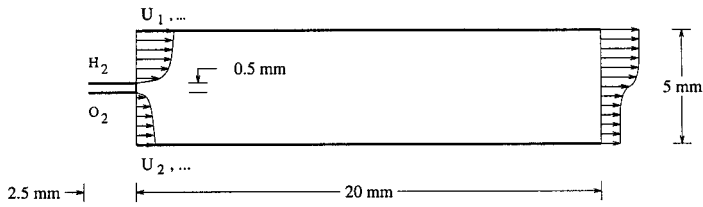


FIG. 13. Physical model employed for the analysis of high-pressure hydrogen/oxygen mixing and combustion processes.

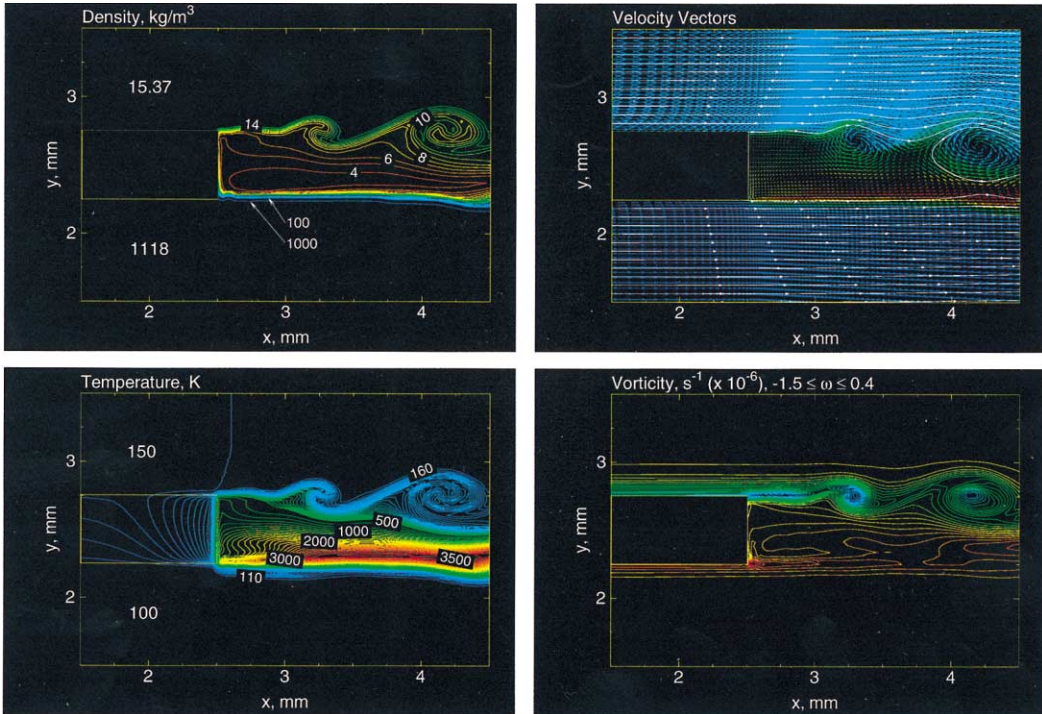


FIG. 14. Contours of density and temperature in the near-field region for transcritical mixing [58].

resultant interactions cause disturbances that grow and coalesce immediately downstream of the splitter plate on a scale that is of the same order of magnitude as the splitter plate thickness. Combined effects induce increased unsteadiness with respect to the flame-holding mechanism and produce significant oscillations in the production rates of H_2O and OH radicals. The temperature within the recirculation zone also fluctuates about the stoichiometric value, with relatively cooler temperatures observed immediately downstream.

Conclusions

Fundamentals of high-pressure transport and combustion processes in contemporary liquid-fueled

propulsion and power-generation systems were discussed. Emphasis was placed on the development of a systematic approach to enhance basic understanding of the underlying physiochemical mechanisms. Results from representative studies of droplet vaporization, spray-field dynamics, and mixing and combustion processes were presented to lend insight into the intricate nature of the various phenomena observed. In addition to all of the classical issues for multiphase chemically reacting flows, a unique set of challenges arises at high pressures from the introduction of thermodynamic nonidealities and transport anomalies near the critical point. The situation becomes even more complex with increasing pressure because of an inherent increase in the flow Reynolds number. The resulting flow dynamics and transport processes exhibit characteristics distinct

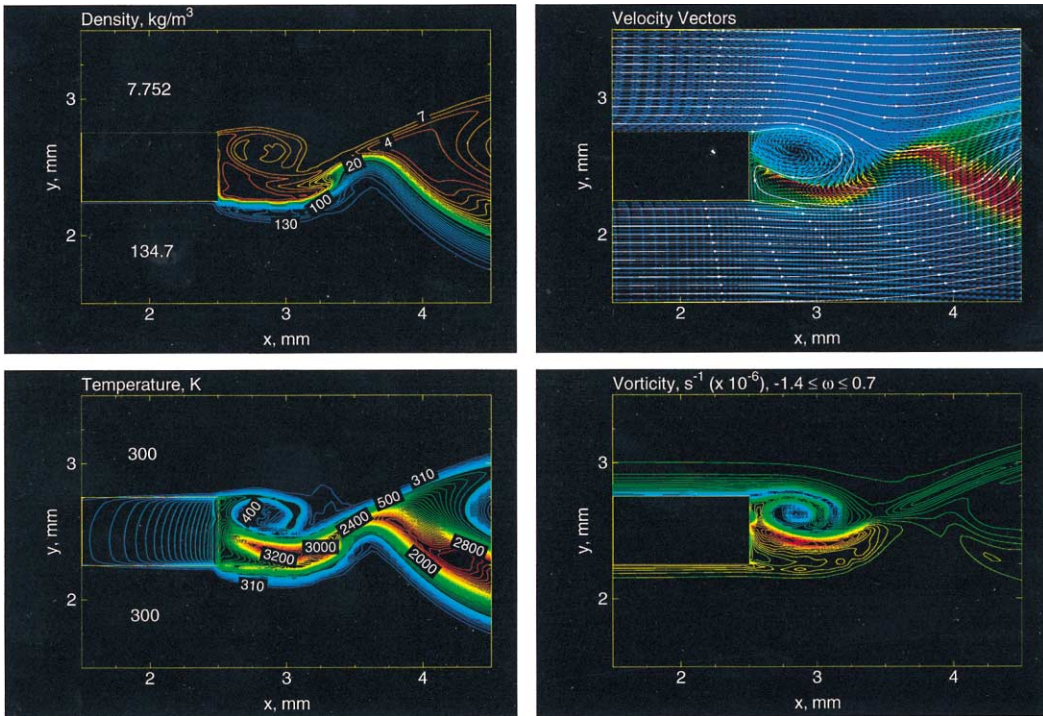


FIG. 15. Contours of density and temperature in the near-field region for supercritical mixing [58].

from those observed at low pressures. In spite of the encouraging, but limited, results obtained to date, the current database is not adequate with respect to quantitative assessments due to the difficulties in conducting experimental diagnostics. The theoretical efforts are similarly deficient because of a lack of validated theories and limited computational resources. Much effort needs to be expended to overcome these obstacles.

Acknowledgments

The author owes a large debt of gratitude to his colleagues and former students, especially Joe Oefelein, George Hsiao, Patric Lafon, Norman Lin, and J. S. Shuen. The paper would not have been completed without their hard work, support, and intellectual stimulation. The work was sponsored partly by the Pennsylvania State University, partly by the U.S. Air Force Office of Scientific Research, and partly by the NASA Marshall Space Flight Center.

REFERENCES

- Spalding, D. B., *ARS J.* 29:828–835 (1959).
- Rosner, D. E., *AIAA J.* 5:163–166 (1967).
- Brzustowski, T. A., *Can. J. Chem. Eng.* 43:30–36 (1965).
- Chervinsky, A., *AIAA J.* 7:1815–1817 (1969).
- Polymeropoulos, C. E., and Peskin, R. L., *Combust. Sci. Technol.* 5:165–174 (1972).
- Manrique, J. A., and Borman, G. L., *Int. J. Heat Mass Transfer* 12:1081–1094 (1969).
- Lazar, R. S., and Faeth, G. M., *Proc. Combust. Inst.* 13:801–811 (1970).
- Canada, G. S., and Faeth, G. M., *Proc. Combust. Inst.* 15:418–428 (1974).
- Rosner, D. E., and Chang, W. S., *Combust. Sci. Technol.* 7:145–158 (1973).
- Kadota, T., and Hiroyasu, H., *Bull. Jpn. Soc. Mech. Eng.* 1515–1521 (1976).
- Hsieh, K. C., Shuen, J. S., and Yang, V., *Combust. Sci. Technol.* 76:111–132 (1991).
- Curtis, E. W., and Farrel, P. V., *Combust. Flame* 90:85–102 (1992).
- Jia, H., and Gogos, G., *J. Thermophys. Heat Transfer* 6:739–745 (1992).
- Delpanque, J. P., and Sirignano, W. A., *Int. J. Heat Mass Transfer* 36:303–314 (1993).
- Jiang, T. L., and Chiang, W. T., *Combust. Flame* 97:17–34 (1994).
- Jiang, T. L., and Chiang, W. T., *Combust. Flame* 97:355–362 (1994).
- Daou, J., Haldenwang, P., and Nicoli, C., *Combust. Flame* 153–169 (1995).
- Shuen, J. S., Yang, V., and Hsiao, G. C., *Combust. Flame* 89:299–319 (1992).
- Yang, V., Lin, N. N., and Shuen, J. S., *Combust. Sci. Technol.* 97:247–270 (1994).

20. Hsiao, G. C., "Supercritical Droplet Vaporization and Combustion in Quiescent and Forced-Convective Environments," Ph.D. thesis, The Pennsylvania State University, University Park, PA, 1995.
21. Lafon, P., "Modélisation et Simulation Numérique de L'Evaporation et de la Combustion de Gouttes à Haute Pression," Ph.D. thesis, à L'Université D'Orléans, 1995.
22. Lafon, P., Yang, V., and Habiballah, M., AIAA paper 95-2432.
23. Haldenwang, P., Nicoli, C., and Daou, J., *Int. J. Heat Mass Transfer* 39:3453-3464 (1996).
24. Meng, H., and Yang, V., AIAA paper 98-3537.
25. Harstad, K., and Bellan, J., *Int. J. Heat Mass Transfer* 41:3537-3550 (1998).
26. Harstad, K., and Bellan, J., *Int. J. Heat Mass Transfer* 41:3551-3558 (1998).
27. Harstad, K., and Bellan, J., *Int. J. Heat Mass Transfer* 42:961-970 (1999).
28. Harswtad, K., and Bellan, J., *Int. J. Multiphase Flow* 26:1675-1706 (2000).
29. Umemura, A., *Proc. Combust. Inst.* 26:463-471 (1986).
30. Umemura, A., and Shimada, Y., *Proc. Combust. Inst.* 26:1621-1628 (1996).
31. Umemura, A., and Shimada, Y., *Proc. Combust. Inst.* 27:2659-2665 (1998).
32. Givler, S. D., and Abraham, J., *Prog. Energy Combust. Sci.* 22:1-28 (1996).
33. Bellan, J., *Prog. Energy Combust. Sci.* 26:329-366 (2000).
34. Jacobsen, R. T., and Stewart, R. B. J., *J. Phys. Chem. Ref. Data* 2:757-922 (1973).
35. Prausnitz, J. M., Lichtenthaler, R. N., and de Azevedo, E. G., *Molecular Thermodynamics of Fluid-Phase Equilibria*, Prentice-Hall, Englewood Cliffs, NJ, 1986.
36. Perry, R. H., Gree, D. W., and Maloney, J. O., *Perry's Chem. Eng. Handbook*, McGraw-Hill, New York, 1984.
37. Ely, J. F., and Hanley, H. J. M., *Ind. Eng. Chem. Fundamentals* 20:323-332 (1981).
38. Ely, J. F., and Hanley, H. J. M., *Ind. Eng. Chem. Fundamentals* 22:90-97 (1983).
39. Sychev, V. V., Vasserman, A. A., Kozlov, A. D., and Spiridonov, G. A., *Property Data Update* 1:529-536 (1987).
40. Ely, J. F., *J. Res. Nat. Bur. Stand.* 6:597-604 (1981).
41. Vesovic, V., and Wakeham, W. A., "Transport Properties of Supercritical Fluids and Fluid Mixtures," in *Supercritical Fluid Technology* (T. J. Bruno and J. F. Ely, eds.), CRC Press, Boca Raton, FL, 1991, p. 253.
42. Levelt Sengers, J. M. H., "Thermodynamics of Solutions Near the Solvent's Critical Point," in *Supercritical Fluid Technology* (T. J. Bruno and J. F. Ely, eds.), CRC Press, Boca Raton, FL, 1991, p. 25.
43. Takahashi, S., *J. Chem. Eng. (Japan)* 7:417-420 (1974).
44. Lafon, P., Yang, V., and Habiballah, M., *J. Fluid Mech.*, in press (2001).
45. Hsiao, G. C., and Yang, V., AIAA paper 95-0383.
46. Yang, V., Habiballah, M., Hulka, J., and Popp, M. (eds.), *Liquid-Propellant Rocket Combustion Devices, Progress in Aeronautics and Astronautics*, AIAA, Washington, DC, 2001.
47. Faeth, G. M., Dominics, D. P., Tulpinsky, J. F., and Olson, D. R., *Proc. Combust. Inst.* 12:9-18 (1960).
48. Sato, J., Tsue, M., Niwa, M., and Kono, M., *Combust. Flame* 82:142-150 (1990).
49. Sato, J., AIAA paper 93-0813.
50. Prakash, S., and Sirignano, W. A., *Int. J. Heat Mass Transfer* 23:253-268 (1995).
51. Ranz, W. E., and Marshall, W. R., *Chem. Eng. Proc.* 48:141-146 (1952).
52. Chen, L. W., and Yuen, M. C., *Combust. Sci. Technol.* 14:147-154 (1976).
53. Renszibulut, M., and Haywood, R. J., *Int. J. Multiphase Flow* 14:189-202 (1988).
54. Chiang, C. H., Raju, M. S., and Sirignano, W. A., *Int. J. Heat Mass Transfer* 35:1307-1324 (1992).
55. Yang, V., and Anderson, W. E. (eds.), *Liquid Rocket Engine Combustion Instability, Vol. 169, Progress in Aeronautics and Astronautics*, AIAA, Washington, DC, 1995.
56. Oefelein, J. C., and Yang, V., *Prog. Aeronaut. Astronaut.* 171:263-304 (1996).
57. Oefelein, J. C., "Simulation and Analysis of Turbulent Multiphase Combustion Processes at High Pressures," Ph.D. thesis, The Pennsylvania State University, University Park, PA, 1997.
58. Oefelein, J. C., and Yang, V., *J. Prop. Power* 14:843-857 (1998).
59. Mayer, W., and Tamura, H., *J. Prop. Power* 12:1137-1147 (1996).
60. Mayer, W. O. H., Schik, A. H. A., Vielle, B., Chauveau, C., Gokalp, I., Talley, D. G., and Woodward, R. D., *J. Prop. Power* 14:835-842 (1998).
61. Mayer, W., Ivancic, B., Schik, A., and Hornung, U., AIAA paper 98-3685.
62. Ivancic, B., Mayer, W., Kruelle, G., and Brueggemann, D., AIAA paper 99-2211.
63. Candel, S., Herding, G., Snyder, R., Scoufflaire, P., Rolon, C., Vingert, L., Habiballah, M., Grisch, F., Pealat, M., Bouchardy, P., Stepowski, D., Cessou, A., and Colin, P., *J. Prop. Power* 14:826-834 (1998).
64. Kendrick, D., Herding, G., Scoufflaire, P., Rolon, C., and Candel, S., *Combust. Flame* 118:327-339 (1999).
65. Woodward, R. D., and Talley, D. G., AIAA paper 96-0468.
66. Hutt, J. J., and Cramer, J. M., AIAA paper 96-4266.
67. Erlebacher, G., Hussaini, M. Y., Speziale, C. G., and Zang, T. A., *J. Fluid Mech.* 238:155-185 (1992).
68. Faeth, G. M., *Prog. Energy Combust. Sci.* 13:293-345 (1987).

COMMENTS

Josette Bellan, Jet Propulsion Laboratory, USA. My first question regards your terminology of *supercritical vaporization*. Since, under supercritical conditions, the latent heat is null, there cannot be vaporization. Please explain. My second question regards the calculation of transport properties such as the diffusivity and the thermal diffusion factors for multicomponent mixtures at high pressures. Are you aware of established methodologies for the reliable calculation of these transport properties for multicomponent mixtures at high pressures? We should note that a single species fuel burning in air constitutes already at least a five-component mixture under the conservative assumption that combustion is complete and thus its products are water and carbon dioxide.

Author's Reply. For simplicity, supercritical vaporization in the present paper refers to vaporization of liquid droplets in supercritical environments. Calculations of thermodynamic and transport properties for multicomponent mixtures at high pressures are discussed in great detail in

the paper. In general, thermodynamic and transport properties except mass diffusivity can be treated reasonably well by means of the corresponding-state principles. Estimation of mass diffusivity remains a challenging task due to the lack of a formal theory or even a theoretically based correlation. Only moderate success was achieved by Takahashi (Ref. [43] in this paper) for the limited number of cases studied.

•

Yaakov Timnat, Techion, Israel. Could you comment on the type of equation of state you recommend to use for obtaining the best results?

Author's Reply. As discussed in the paper, the Benedict-Webb-Rubin equation of state in conjunction with the corresponding-state principles provides the best result of fluid p - V - T properties over all the fluid thermodynamic states, from compressed liquid to dilute gas.